Supplementary Note to 'Hund's coupling mediated multi-channel quantum phase transition of a single magnetic impurity in Fe(Se,Te)'

M. Uldemolins[1], A. Mesaros[1], G. D. Gu[2], A. Palacio-Morales[1], M. Aprili[1], P. Simon[1] & F. Massee[1]

[1] *Université Paris-Saclay, CNRS, Laboratoire de Physique des Solides, 91405, Orsay, France*
[2] *Condensed Matter Physics and Materials Science Department, Brookhaven National Laboratory, Upton, NY 11973, USA*

Supplementary Note 1

In this Supplementary Note we discuss the robustness of the observations made in the main text to variations in the model parameters and show additional experimental observations. We start by noting one consequence of the nature of the multi-channel QPT: since the excitations involve transitions between different states before and after the QPT (and not a simple crossing as in the classical YSR model), the lowest-lying excitation does not need to cross zero-bias energy at the transition. Hence, the crossing in the theoretical model is not protected but depends on the parameters. For main text Fig. 3 we choose to present a situation where the energy of the first excitation satisfies that $E_{|1/2,-,+\rangle} - E_{\mathrm{GS}} \simeq 0$ at the MCQPT, and there is a zero-bias crossing in the sub-gap LDOS. We stress, however, that there exists a wide region in the parameter space, within the already introduced model assumptions of main text Eqs. (2),(3), for which the gap in the lowest-lying-excitation energy is below the experimental resolution, see Fig. S1. As the figure shows, the requirement of observing the crossing within resolution imposes a quite natural condition that the tunneling rates for the two orbitals are of the same order of magnitude, and the coupling of orbital to substrate is larger than the superconducting gap.

Experimentally, the several examples of transitions we identify all show the crossing, at least within the experimental energy resolution. Given that all analyzed impurities have the same nature (surface excess iron atoms), it is expected that they are described by sets of parameters that are close to each other in parameter space, and therefore it is not surprising that all impurities exhibiting a transition show an analogous behavior (as it happens, an apparent crossing).

In Fig. S2 (a-c) we give an example of the opposite scenario, where the MCQPT clearly lacks a zero-energy crossing. We emphasize that our MCQPT in absence of crossing still has the other essential features: the large change of the average orbital occupation at the transition, which yields a simultaneous change in the polarity of all in-gap states (from hole-like to electron-like), as well as the possibility of NDC that is discussed in Supplementary Note 2.

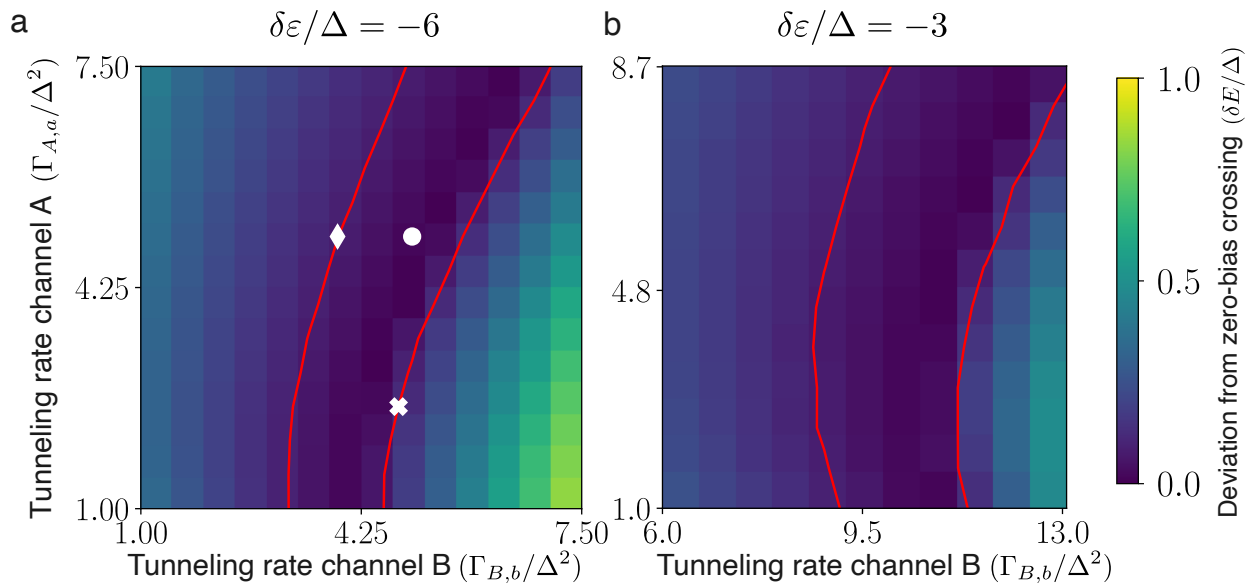

Figure S1 Magnitude of the gap in the lowest-lying excitation (i.e., deviation from a zero-bias crossing) at the MCQPT for **a**: $\delta\varepsilon/\Delta = -6$, and **b**: $\delta\varepsilon/\Delta = -3$. The rest of the parameters are the same in both plots ($U = 60$, $J = 30$, in units of Δ), but note that the axes span a slightly different range. The red contours correspond to $\delta E/\Delta = 0.08$, i.e. the experimental resolution $\delta E \equiv 3.5 k_{\mathrm{B}} T$ for $\Delta = 1.5$ meV and electron temperature $T = 0.4$ K. A relatively large parameter range is chosen since assessing precisely its size (e.g. from the experiment or ab initio simulations) is impossible given the minimal nature of the model. The markers in (a) correspond to various choices of the tunneling rates presented in the text: Fig. 3 in the main text (circle) and Fig. S2 (diamond and cross).

We also note that there exists an additional variation of the MCQPT which in principle yields a discontinuous in-gap LDOS. Namely, the system can undergo two consecutive QPTs of the ground state, from $|0, +, +\rangle$ into $|1/2, -, +\rangle$, and subsequently, from $|1/2, -, +\rangle$ into $|1, -, -\rangle$. Far away from the transition, the level ordering is analogous to that of the scenario discussed so far, and crucially, the impurity also experiences a large change of the occupation (see Fig. S2 (d-f)). There exists again a wide region in the parameter space in which these two QPTs are sufficiently close in $\bar{\varepsilon}$, so that they result in an in-gap LDOS indistinguishable from the scenario discussed above, i.e., with a crossing observed within the energy resolution.

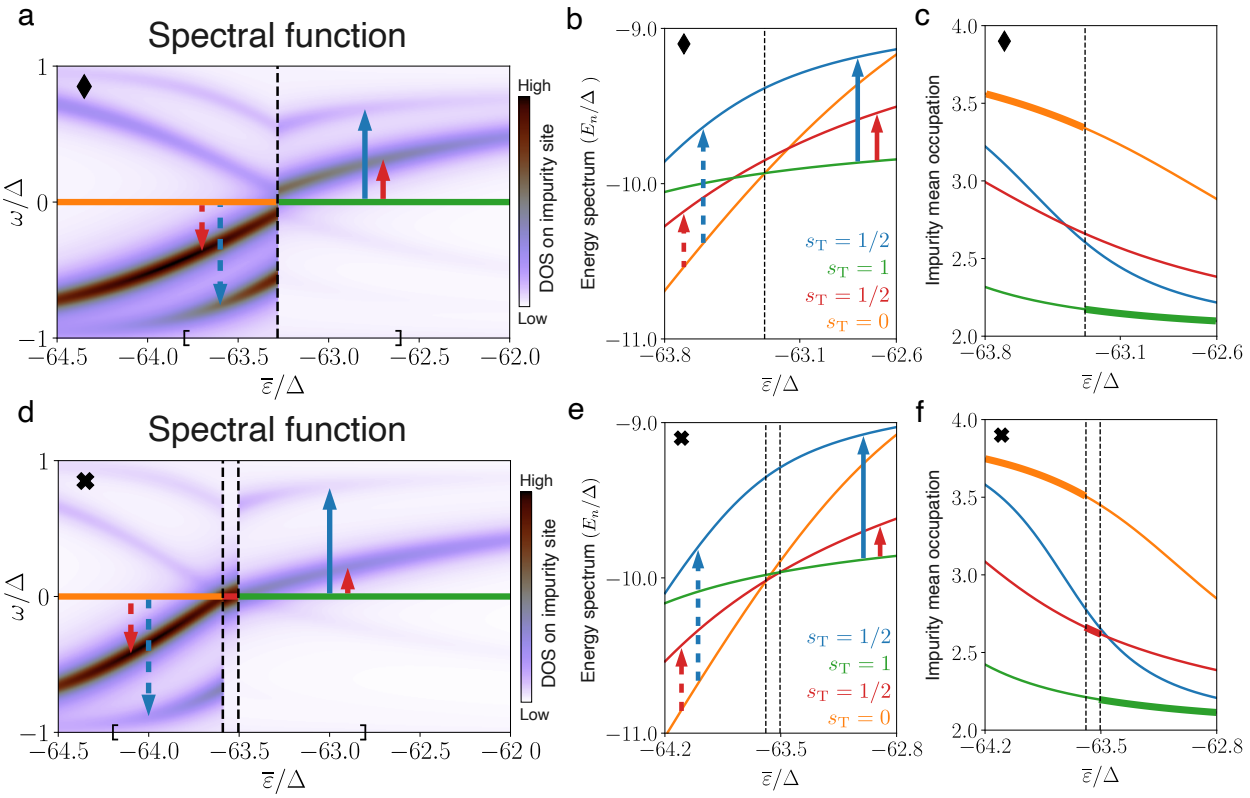

Figure S2 **Robustness of the MCQPT**. Top row: **a** Simulated in-gap LDOS at the impurity site as a function of $\overline{\varepsilon}/\Delta$. **b** Evolution of the energy of the four lowest-lying many-body states. **c** Evolution of the average total electron occupation on the impurity for all four many-body state. The color-coding and the arrows are the same as in main text Fig. 3. The parameters correspond to the diamond marker in Fig. S1. Bottom row: Same as top row but with tunneling rates corresponding to the cross marker in Fig. S1. In this case, the deviation from zero-bias crossing $\delta E/\Delta$ is defined as the separation of the two QPT (black dashed lines), which yields a discontinuity in the in-gap excitations.

Finally, we reiterate that since the single-particle excitations in the in-gap LDOS result from different eigenstates before and after the MCQPT, in general there is a discontinuity of slope and the amplitude of the in-gap state energy at the point it crosses zero-bias. As Fig. S3 shows for two different Fe impurities, this is indeed the case in our experimentally observed MCQPT.

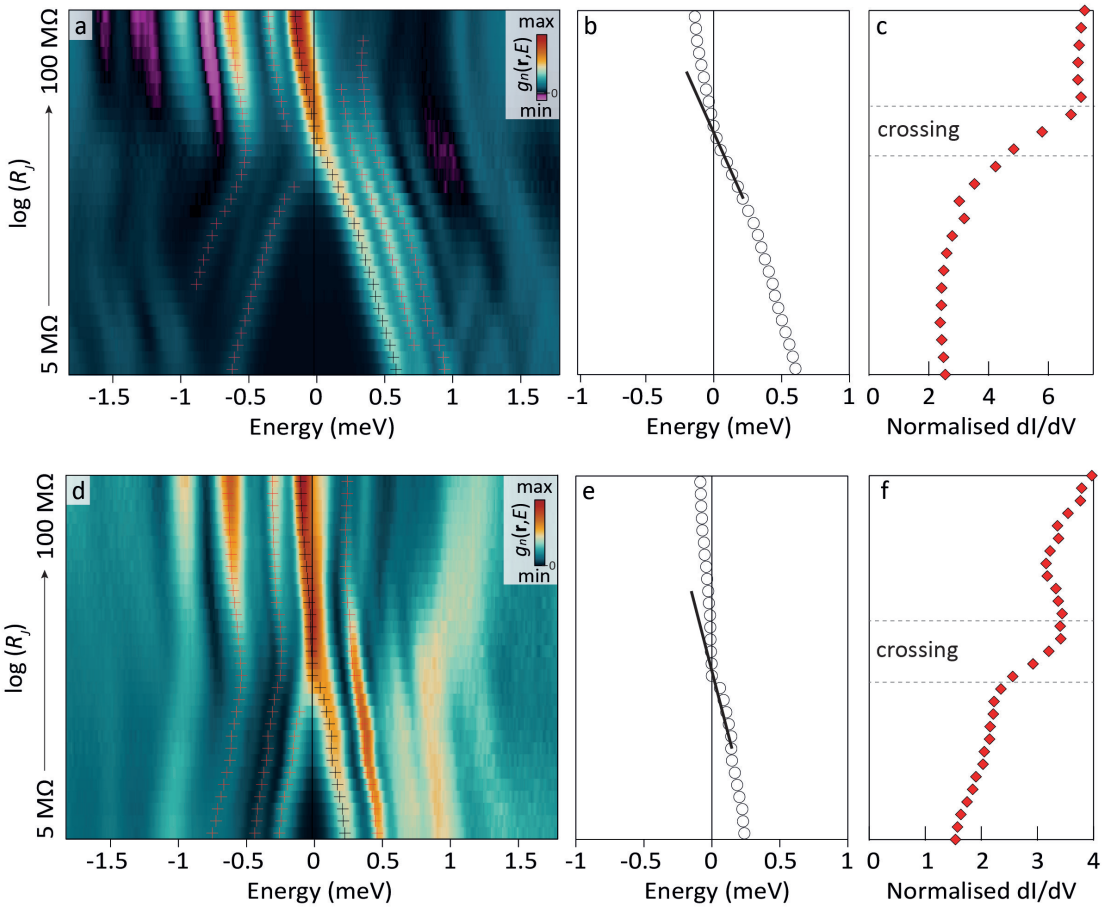

Figure S3 Slope and amplitude change upon crossing E = 0. **a** Normalized differential conductance spectra taken at different junction resistances on the same excess Fe atom as in main text Fig. 2. Crosses are fitted locations of the most prominent peaks. The junction resistances run from 5-100 MΩ on a logarithmic scale. **b** Fitted peak voltages for the in-gap state that crosses E = 0. The line indicates the slope of the in-gap energy versus junction resistance after crossing E = 0. **c** Amplitude of the peak that crosses. Upon crossing, both the slope and the amplitude change. **d** - **f** Same as a - c for another excess Fe impurity. Again, upon crossing E = 0, the slope and amplitude change.

Supplementary Note 2

A comprehensive numerical transport calculation starting from our initial 2-orbital Anderson impurity model that would include both the STM tip and the superconducting substrate is beyond the scope of this paper. Instead, in this Supplementary Note we present a minimal phenomenological transport calculation that may account for the negative differential conductance (NDC) observed in the STM measurements.

It is important to note that our STS experiment is probing bound states with some finite spatial extent, centred at the magnetic impurity. These bound states are furthermore well inside the superconducting gap and as such isolated from other states. Additionally, the experiment is carried out in the tunneling regime such that elastic Andreev processes are negligible. To account for the physics of transport we hence switch from the detailed description of impurity orbitals to a phenomenological modelling of the isolated in-gap bound states as states located in a quantum dot-like box.

As it was noted in Ref. [1], NDC in multi-channel quantum-dot like systems originates from a combination of the Coulomb interaction and an asymmetrically-suppressed coupling to the reservoir. Inspired by these results, we postulate that some of the in-gap bound states are asymmetrically and weakly coupled to the STM tip, therefore, their spectral footprint becomes a NDC peak in the transport calculation.

To explain the experimental observations, we approximate tunneling into the in-gap bound states emerging from a complex impurity-superconductor system as tunneling into simple energy levels. Specifically, we phenomenologically introduce a spinless two-level interacting model,

$$H_{\text{eff}} = \sum_{l=1,2} E_l \hat{n}_l + K \hat{n}_1 \hat{n}_2, \tag{1}$$

with $\hat{n}_l$ the particle-number operator. The energy levels in this effective toy model should be interpreted as the in-gap bound states stemming from the magnetic impurity, but existing in the superconducting substrate; they should not be confused with the orbital energy levels in the MCAIM of the impurity employed to explain the very emergence and behaviour of these in-gap bound states.

The phenomenological correspondence between the impurity and the bound states implies that the re-ordering of the many-body states as we tune the system through the multi-channel QPT is reflected into a re-ordering of the energy levels in the effective model (see Fig. S4). In addition, K should be interpreted as an effective repulsive interaction which penalizes double occupation of the bound states.

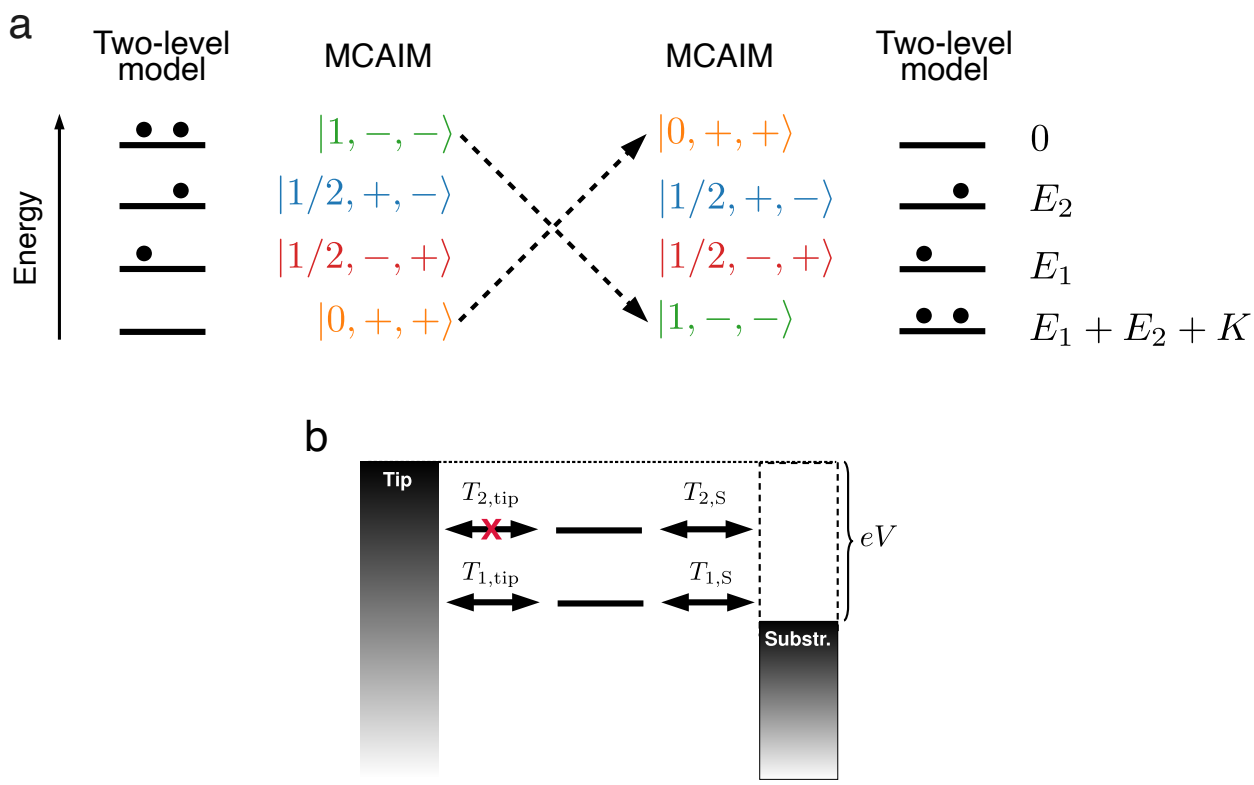

Figure S4 Effective two-level model to account for the NDC. a Schematic phenomenological correspondence between the energy levels in the effective model and the lowest-lying many-body eigenstates in the multi-channel Anderson impurity model. The arrow crossing indicates the MCQPT. **b** Schematic of the transport model. The coupling between the left reservoir and level 2 is strongly suppressed.

Further, we couple the two-level system to two reservoirs which describe the substrate and the STM tip respectively. Crucially, we assume that one of the couplings between the tip and one of the bound state wavefunctions is strongly suppressed; this could be for example due to symmetry reasons. It has been shown experimentally that the bound state wavefunction shares the same symmetry as the orbital it originates from [2,3]. Although our data on Fe(Se,Te) show no clear orbital character, which is possibly masked/lifted by gap and/or Se/Te inhomogeneity, position dependent tip gating, inter-level interactions, or the strong J_H itself, they are strongly varying as function of energy and position, and spatially asymmetric. Therefore, we can easily imagine a small matrix element between the tip wavefunction and one bound state wavefunction originating from an orbital with an orthogonal symmetry. In the following, we therefore assume ($T_{1,\mathrm{S}} = T_{2,\mathrm{S}}$ and $T_{1,\mathrm{tip}} \gg T_{2,\mathrm{tip}}$). For the sake of simplicity we also assume that $T_{1,\mathrm{S}} = T_{1,\mathrm{tip}}$ but our results do not depend on the latter condition.

Finally we assume that all the coupling strengths are much smaller than the temperature, $T_{l,r} \ll k_{\mathrm{B}}T$, with $l = 1, 2$ and $r = \mathrm{S}, \mathrm{tip}$, as the bound state broadening in the experiment is related to the experimental temperature. We emphasize again that the couplings $T_{l,r}$ are not directly related

to the couplings between the impurity and the superconducting site in the MCAIM $\Gamma_{i,\alpha}$, which are typically larger than Δ, but instead to the intrinsic broadening of the bound states which is typically much smaller than the temperature. Indeed, STS experiments on magnetic impurities in superconductors have confirmed that the intrinsic intra-gap bound state energy broadening is typically much smaller than the temperature (see Refs. [4–7], supporting this assumption).

In Fig. S5 we present the differential conductance calculated numerically for this effective phenomenological toy model with a numerical method based on the Lindblad equation (resulting from an approximate master equation approach) implemented in the python package QmeQ 1.0 [8]. It is worth pointing out that the use of the Lindblad method crucially relies on the fact that the temperature is larger that the intrinsic level broadening as discussed above.

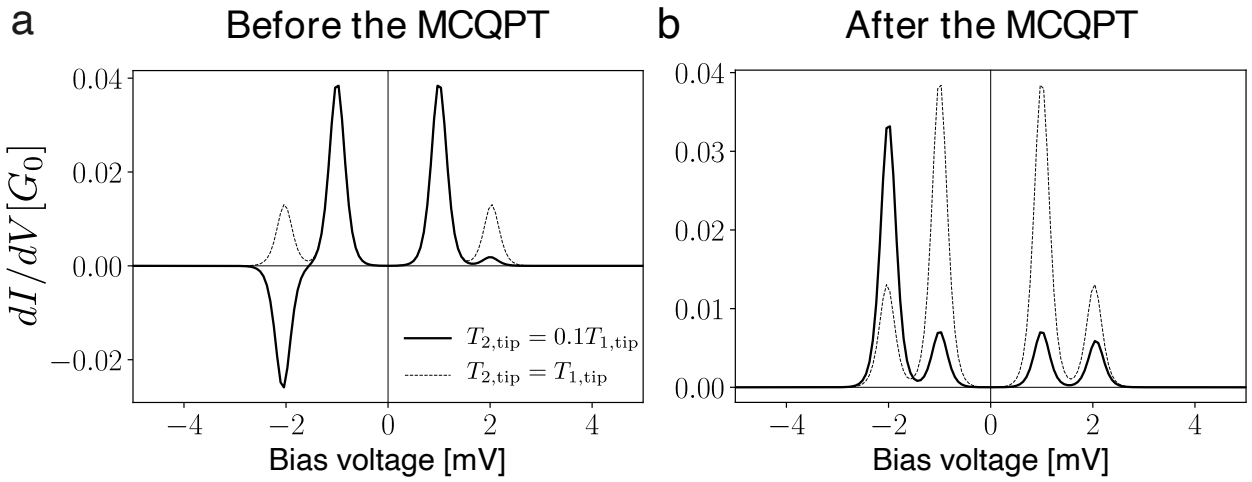

Figure S5 Simulated differential conductance in the effective two-level model. **a** Level ordering analogous to left-hand side of Fig. S4. **b** Level ordering analogous to right-hand side of Fig. S4. Solid (dashed) lines represent assymetric (equivalent) coupling strengths. Only in the former case there can be NDC. Parameters (in meV): (a) $E_1 = 0.5$, $E_2 = 1.0$, $K = 3$, $T_{1,\mathrm{tip}} = 0.005$ (dimensionless), $k_\mathrm{B}T = 0.05$. (b) $E_1 = -4.0$, $E_2 = -3.5$, the rest same as (a).

Before the transition (Fig. S5a), the two lowest-lying peaks in the calculated dI/dV for the effective phenomenological toy model correspond to single-particle transitions from an empty state to single-occupied levels 1 and 2 respectively. If the tunneling rate from the left reservoir (STM tip) to level 2 (an in-gap bound-state) is much smaller than the rest, electrons cannot flow from level 2. Since the large K penalizes the double occupation of level 1, electrons get stuck in level 2. Therefore, the current collapses and the corresponding excitation appears as a NDC peak at negative bias. After the transition (Fig. S5b), the two lowest-lying excitations for the effective toy model correspond to single-particle transitions from a doubly-occupied level to single-occupied levels 1 and 2 respectively. The differential conductance is not negative now, because these transitions involve both levels, therefore, electrons can always escape through level 1.

An important feature of the model above is that the asymmetry in tunneling which causes the NDC does not modify the energies at which the (positive or negative) peaks of the differential conductance occur (see Fig. S5). Consequently, the energy E_{NDC} at which the NDC peak occurs is an excitation energy so that a peak (in principle, either positive or negative) should occur also at $-E_{\mathrm{NDC}}$. Fig. S6 demonstrates on two examples of experimental data where indeed such a matching is observed.

Our effective low-energy phenomenological toy model captures three key features of the MCAIM. First, excitation transitions before and after the MCQPT are from different ground states into the same excited states in both the effective toy model and the MCAIM. Second, the parity of the effective ground states is the same before and after the transition in both models as well. Third, upon assigning $+1/2$ spin to the particles in the toy model, we also relate the change in the spin quantum number in both models.

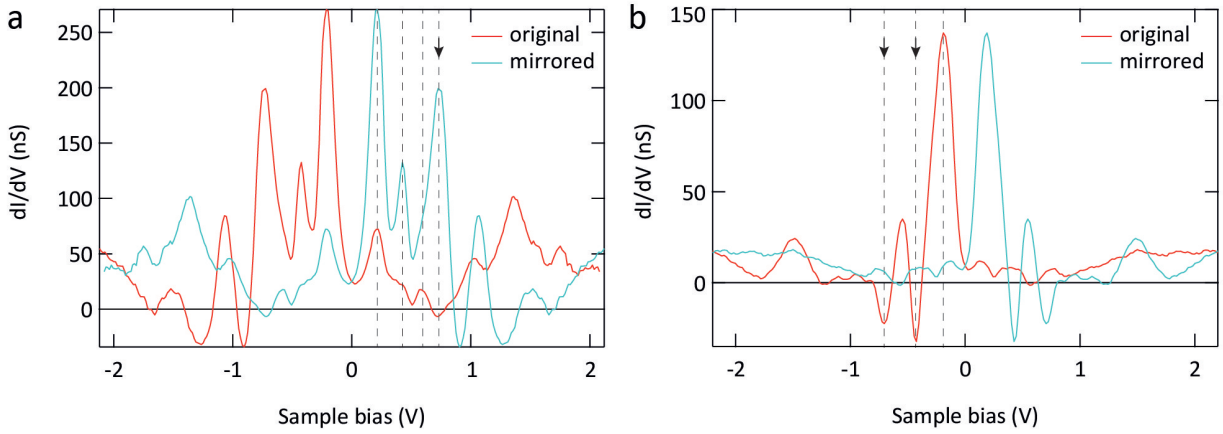

Figure S6 Negative differential conductance spectra. **a**, **b** Differential conductance spectra taken on different excess Fe impurities. For each spectrum, the differential conductance is plotted as function of the bias voltage (red) and its inverse (blue). The arrows indicate several instances where a NDC dip matches a peak at opposite polarity, in agreement with the two-level model in Fig. 5a. We note that not all NDC dips perfectly match a peak at opposite bias, which likely results from (multiple) partially overlapping states with non-zero width.

Supplementary Note 3

For completeness, we note that the QPT in the $J_H = 0$ case is a transition in a single-orbital AIM model for orbital a, from a $s_{\mathrm{tot},a} = 0$ ground state with an occupation above one to a $s_{\mathrm{tot},a} = 1/2$ ground state with a singly-occupied orbital. Hence, although the spin on the impurity behaves as for two independent Kondo models, the occupation of the impurity changes through the MCQPT, which is not captured in the Kondo model. The departure from the Kondo model is expected [9]

since near the MCQPT the impurity is in a mixed-valence regime [see Eq. (3) of main text] and the strong charge fluctuations are driven either by changes in $\bar{\varepsilon}$ or in Γ. Naturally, deep in the large-spin configuration, a description within the Kondo paradigm would become suitable, where the large Hund's coupling is expected to yield low Kondo temperature(s) [10] likely smaller than the superconducting gap. For completeness, we note that the parameter choice of the simulation presented in the main text is consistent with a negligibly small Kondo temperature, $T_{\mathrm{K}} \sim e^{-1/\rho_0|J_{\mathrm{K}}|}$: the density of states at the Fermi level, $\rho_0 \sim 2.5$ eV^{-1} [11,12], yields $\rho_0|J_{\mathrm{K}}| \sim 5 \cdot 10^{-3}$, with J_{K} estimated from the standard single-orbital Anderson model [13]. Consistent with these estimates of a low T_{K}, our data away from the MCQPT, hence possibly deep in the large-spin configuration, does not show obvious signs of a Kondo resonance, and we are unable to provide an experimental analysis of the T_{K}/Δ ratio in such a regime. Nevertheless, we emphasize that the MCQPT discussed in this work is strongly tied to a mixed-valence state of the impurity, where Kondo physics is not applicable.

Supplementary Note 4

In this Supplementary Note we show additional spectroscopy data and examples of zero energy crossings, and discuss in more detail negative dI/dV, and gating as proposed mechanism of peak shifting.

Negative differential conductance. As the main text experimental figures and additional spectra in Fig. S7 show, negative differential conductance (NDC) is observed on a large subset of excess Fe atoms (well over 50% of the Fe atoms we studied). If the NDC is not found on the centre of the Fe atom, it often appears slightly off-centre (see Fig. S7) and can furthermore be junction resistance dependent (see e.g. main text Fig. 2). We stress that NDC with a normal metal tip is not a common occurrence and typically requires interacting channels.

This is unlike for superconducting tips, where NDC is readily observed because instead of a flat tip DOS, the superconducting coherence peaks of the tip act as filter leading to a strong increase in the current upon aligning one of the coherence peaks with a sub-gap state, and subsequent drop in current upon passing the sub-gap state. Interestingly, as Ref. [4] shows, a superconducting tip can in some cases also lead to a switch in particle-hole asymmetry of sub-gap states as function of junction resistance. We stress, however, that this is not the case for a normal metal tip [4].

Despite characterizing our W tip on a Pt crystal before the measurements, there is nonzero probability of picking up a small piece of Fe(Se,Te), thereby making the tip superconducting as well. The energy of our coherence peaks, however, is similar to that observed by others using normal metal tips. As e.g. detailed in Ref. [14], multiple coherence peaks are typically observed, and the peak-to-peak energy separation displays a considerable spatial variation. Our spectrum in main text Fig. 1 falls on the larger end of this variation without the need to invoke an additional gapping due to a superconducting tip.

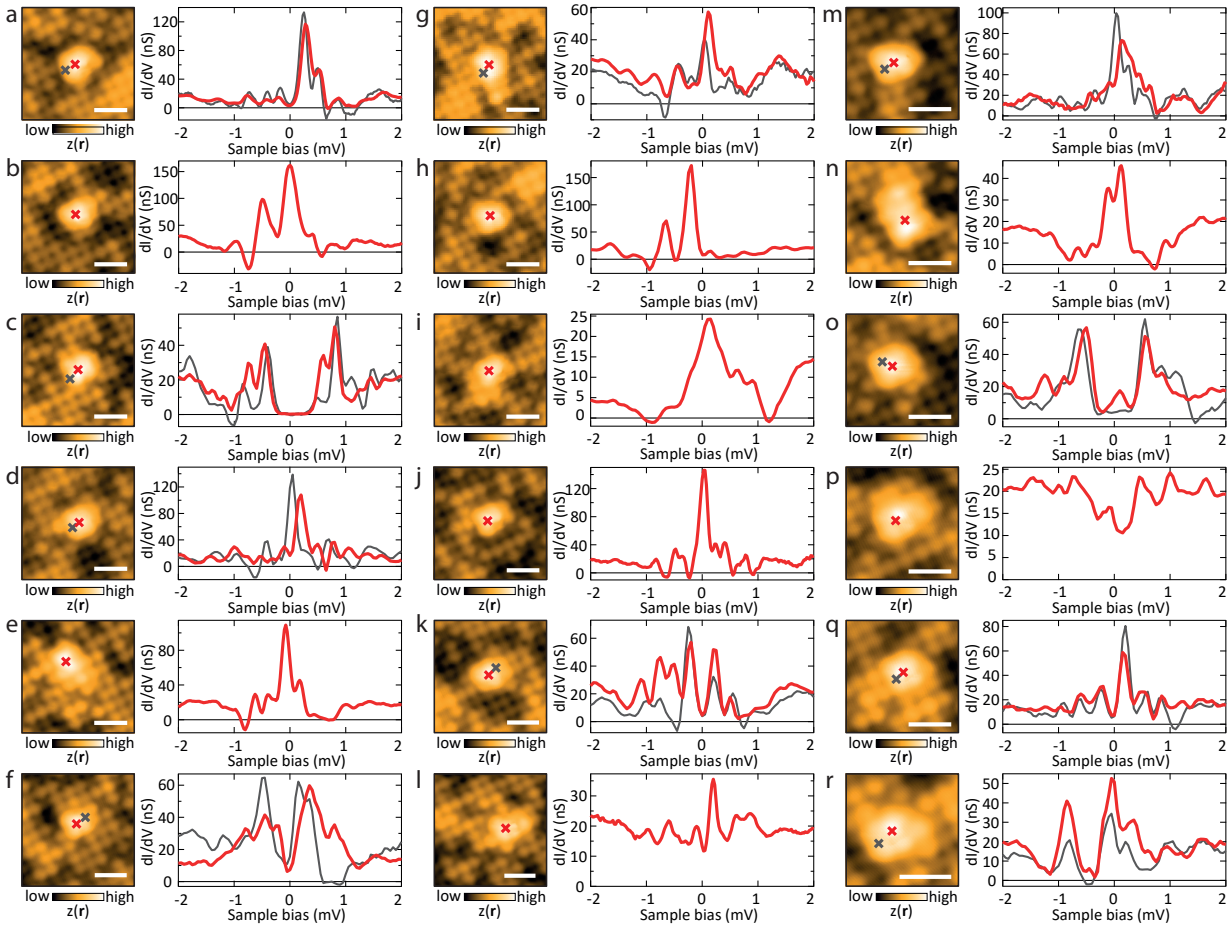

Figure S7 Spectra on various Fe. **a-r** Constant current image (left) and differential conductance spectrum (right) of 18 different excess Fe atoms. For those Fe atoms where the core (red spectrum and cross) does not show negative differential conductance, a spectrum slightly off-centre usually does (grey spectrum and cross). We note that of all our excess Fe atoms, none show a state at zero bias that does not move off-zero with changing tip-sample distance. We therefore have no signatures in our data that requires us to invoke topological superconductivity. $V_{set} = 5$ mV for all data, $I_{set} = 50$ pA (spectrum of i) or 100 pA (everything else). c is the same Fe as main text Fig. 1d; h = Fig. 1b; b = Fig. 2; d = Fig. 1c and Fig. S8a; j = Fig. S3c; g = Fig. S8b.

More generally, we can rule out that the tip is responsible for the NDC. Any tip showing NDC will need to have a sharp feature, which for a superconducting tip are the coherence peaks, but can also be due to e.g. a molecule on the end of a normal tip [15]. Except if there is an unusual orbital selectivity [15], NDC would then be seen on all (sufficiently isolated) sub-gap states, regardless of the polarity, both of which is not the case for us. Additionally, a tip with such a singularity is likely to lead to sharper features in spectroscopy. For example, our data are taken at 0.3 K, whereas those of e.g. Ref. [16] were taken at 1.1 K with a superconducting tip and are much sharper. A superconducting tip will moreover in most cases have a non-zero gap in which case one would

never observe a zero crossing of a sub-gap state. To dispel all doubts, we finally note that we have observed NDC on excess Fe atoms in Fe(Se,Te) with multiple tips on different samples during different cool-downs, highlighting the robustness of our finding.

Gating as mechanism for peak shifts. Previously reported quantum phase transitions have been mostly established by tuning the impurity-substrate coupling using the atomic force between tip and impurity [16–18]. Specifically, MnPc molecules were used, which are relatively large objects that are deposited on top of the surface. In our case, however, such tuning is less likely to be important. First of all, the excess Fe impurities we focus on are relatively strongly bound to the substrate: unlike MnPc we cannot push them around or controllably pick them up. Secondly, for subsurface impurities in Fe(Se,Te), where the force between the tip and impurity is even smaller, sub-gap states in Fe(Se,Te) have also been seen to shift with tip-sample distance (see Ref. [19]). Therefore, instead of a tip-impurity force, a tip gating effect is more likely causing the level shifts as put forth in Ref. [19]. Importantly, the energy scale of such gating is very different to the energy scale of the measurements. Similar to band-bending in semiconductors, the gating depends on the relative work functions, which are in the eV range - orders of magnitude larger than the voltage variations in our measurements. Changing the tip-sample distance in this case will thus to a good approximation shift all levels equally as we have used for our theoretical modelling, and will be independent of the mV voltages we use.

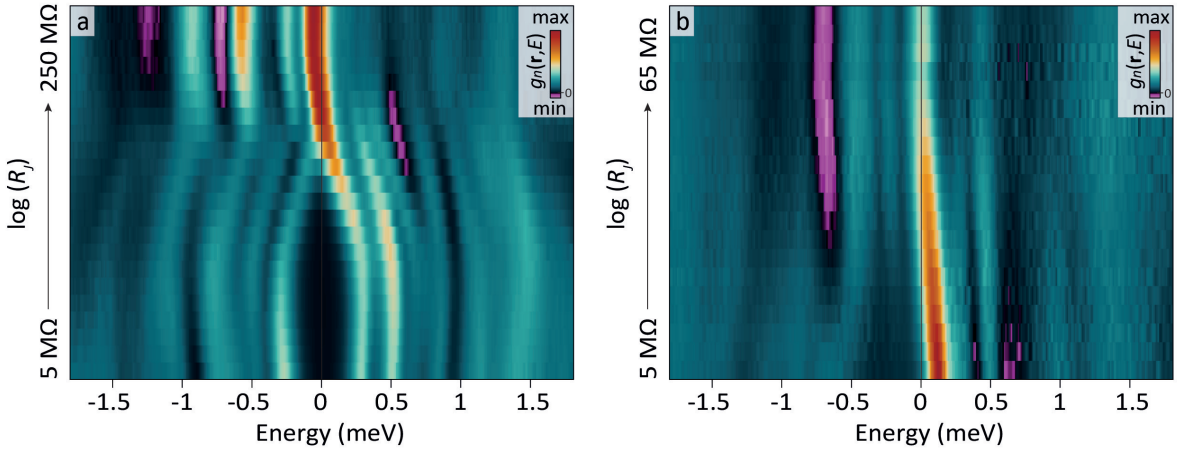

Figure S8 Additional $\mathbf{R}_J$ data. **a**, **b** R_J dependence measurements where a zero crossing occurs on two additional Fe impurities.

In addition to the tens of excess Fe atoms on which we have recorded point spectra, a selection of which is shown in Fig. S7, we have recorded detailed junction resistance dependence measurements on 8 excess Fe atoms including four that display a zero crossing. Two of these four that cross zero energy are shown in Fig. S3, and one of the four that does not cross is shown in main text Fig. 1d. Fig. S8 shows the R_J dependence of the two additional Fe impurities with a zero crossing, which show the same characteristics as the other data where a zero crossing occurs, highlighting the robustness of our observations.

Finally, Fig. S9 shows two examples of junction dependent measurements in cases where none of the sub-gap states crosses zero energy. As these data show, there are nonzero changes in the amplitude of the peaks, which suggests the tunnelling rates into the various sub-gap states have a different tip-impurity distance dependence. These changes, however, are gradual and never lead to a switch in intensity between polarities. Interestingly, particularly the NDC appears sensitive to the tip-impurity distance, in both cases being more pronounced in the normalised curves at high junction resistance, i.e. for low tunnelling rates. This further suggests that NDC occurs due to blocking by a weakly coupled level: for lower junction resistances the blocking level will become more strongly coupled, lifting the NDC.

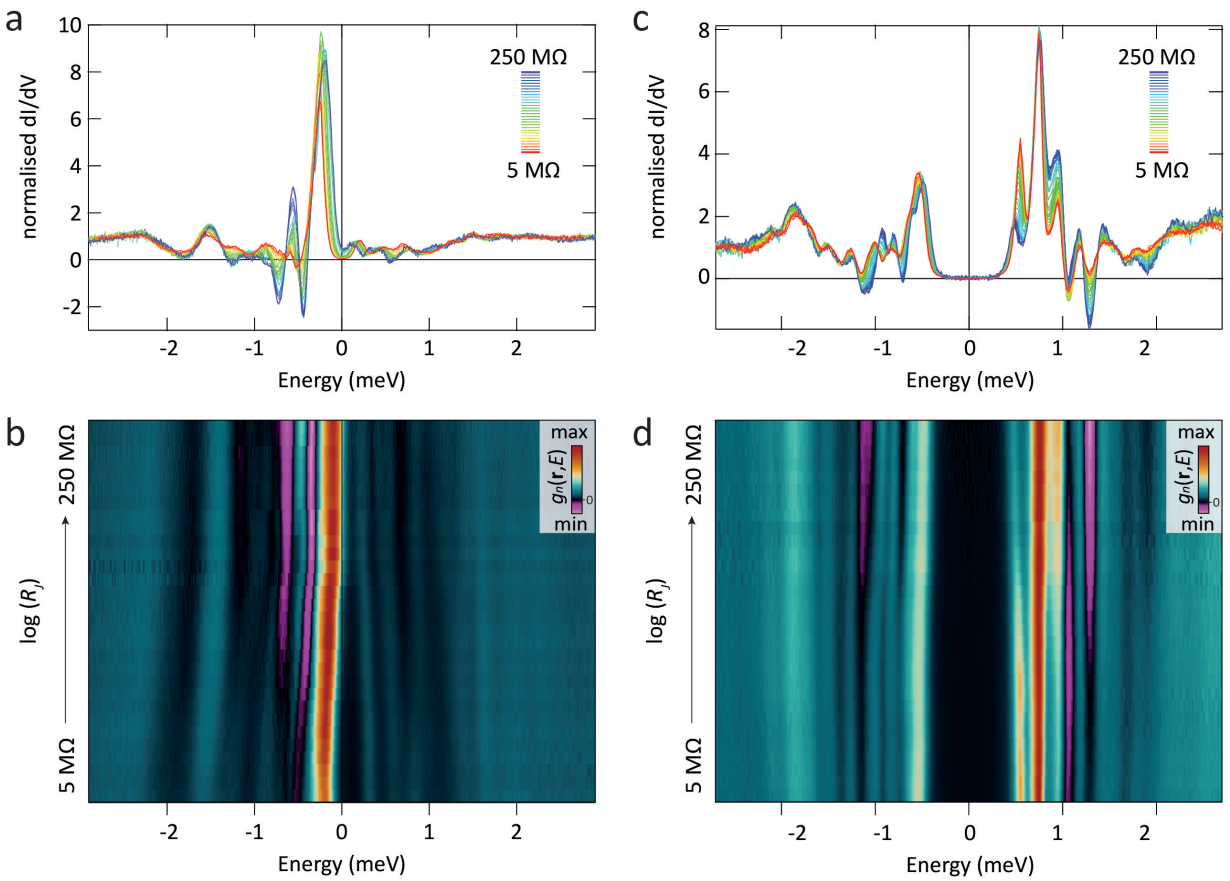

Figure S9 R_J dependencies without crossing. **a** R_J dependence of tunnelling spectra and **b** corresponding 2D visualization on an excess Fe atom where none of the in-gap states cross zero energy. **c-d** The same as **a-b** for the Fe atom shown in main text Fig. 1d, here measured at a slightly different location on the defect. In both cases the in-gap peak amplitudes are relatively constant, ruling out a strongly selective tip-impurity distance orbital dependence, and highlighting that the change in amplitude observed upon a MCQPT is not simply an effect of the change in R_J.

Supplementary Note 5

In this Supplementary Note, we show that the MCQPT characterizing our model can also be triggered by continuously varying the average tunneling rate, $\overline{\Gamma} = (\Gamma_{A,a} + \Gamma_{B,b})/2$, between the impurity and the substrate. Akin to the scenario discussed in the main text, the strong Hund's coupling here also induces a large change in impurity occupation between a low-spin state and a high-spin state, which manifests as a simultaneous change in the polarity of the in-gap excitations (from negative bias to positive bias). We recall that in the AIM the impurity-substrate hybridization competes with the local Coulomb interaction, so that increasing the former hinders the local-moment formation [20]. Therefore, decreasing $\overline{\Gamma}$ should have an analogous effect to making $\overline{\varepsilon}$ less negative. Indeed, as shown in Fig. S10, this correspondence is confirmed, and we observe the entire phenomenology of the MCQPT.

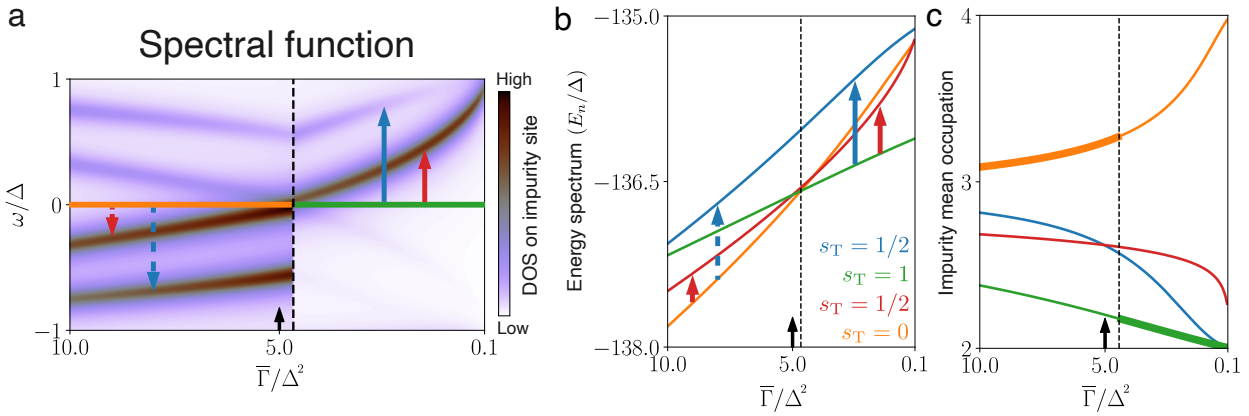

Figure S10 MCQPT driven by varying the tunneling rate $\overline{\Gamma}$. **a** Simulated in-gap LDOS at the impurity site as a function of $\overline{\Gamma}/\Delta^2$. **b** Evolution of the energy of the four lowest-lying many-body states. **c** Evolution of the average total electron occupation on the impurity for all four many-body state. The color-coding and the arrows are the same as in main text Fig. 3 (MTF3). Calculation parameters: J_{H}, U, $\delta\varepsilon$, η same as in MTF3. We set $\overline{\varepsilon}/\Delta = -63.3 < \overline{\varepsilon}_{\mathrm{MCQPT}}$ in MTF3, so that the MCQPT occurs at a higher value of $\overline{\Gamma}/\Delta^2$ than that of MTF3 (indicated by the small black arrow on the horizontal axis). Note that here it is not necessary to shift the energy curves in panel (b) for readability.

Supplementary Note 6

In the main text we show that crossing our MCQPT preserves the total electron parity. Here we elaborate on the fact that this is not a universal feature of the MCQPT, as with more than two impurity orbitals the same phenomenology of the MCQPT may occur while parity does change sign. As a minimal concrete example, let us consider adding to our model a third orbital c coupled to a scattering channel C in the superconductor. For a similar set of parameters as in the two-orbital problem, upon varying the mean impurity energy level, the ground state of the system changes

from $|0,+,+,+\rangle$ to $|3/2,-,-,-\rangle$, with three in-gap states that correspond to excitations into $|1,-,-,+\rangle$, $|1,-,+,-\rangle$, and $|1,+,-,-\rangle$, while the third quantum number indicates the parity in channel c, C. As in the two-orbital scenario discussed in the main text, the system evolves from a higher-occupation/small-spin state into a lower-occupation/high-spin state due to the effect of the Hund's coupling. This transition also manifests as a concurrent flip of the polarity of the in-gap states.

Supplementary Note 7

In this Supplementary Note we show that the fundamental features of the MCQPT are independent of the relationship between the intra-orbital interaction U and the Hund's coupling J_{H}.

Provided that the magnitude of the Hund's coupling is larger than the splitting of the orbital energy levels $\delta\varepsilon$, the simulation of the MCQPT for different U/J_{H} ratios (0.5 and 10 in top and bottom rows of Fig. S11, respectively) exhibits the same phenomenology as the scenario discussed in the main text ($U/J_{\mathrm{H}} = 2$), namely, a large change in the total spin of the ground state and occupation of the impurity, which manifest as a simultaneous change in the polarity of all the in-gap states. The various choices of U presented in this Note make explicit the crucial assumption that the impurity is in a mixed-valence state: in each case, the MCQPT occurs at a different value of $\overline{\varepsilon}$, as expressed in Eq. (3) in the main text. Crucially, the variation in $\overline{\varepsilon}$ required to trigger the MCQPT is independent of U, therefore, the assumption that impurity energy levels vary with the tip-sample distance is not constrained by its specific value.

Following previous studies of iron impurities on FeSe systems [21], we set $|\overline{\varepsilon}|$ and U to be on the order of 100 meV in all the other simulations presented in this work. Further, as the Hund's coupling originates from inter-orbital Coulomb interactions, we chose it to be of the order of U (yet, smaller) [10].

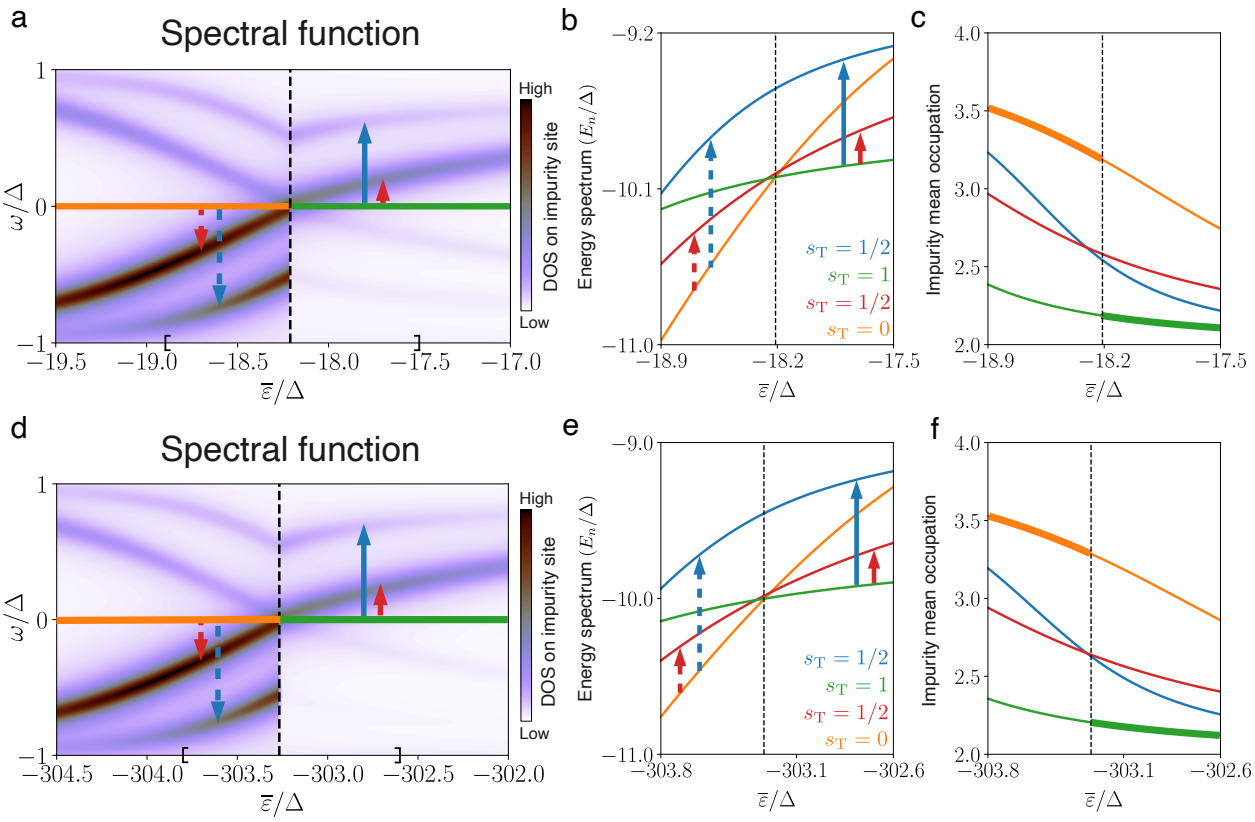

Figure S11 Dependence of the MCQPT on the intra-orbital Coulomb interaction. Top row: **a** Simulated in-gap LDOS at the impurity site as a function of $\overline{\varepsilon}/\Delta$. **b** Evolution of the energy of the four lowest-lying many-body states. **c** Evolution of the average total electron occupation on the impurity for all four many-body states. The color-coding and the arrows are the same as in main text Fig. 3 (MTF3). Calculation parameters: J_{H}, $\delta\varepsilon$, η same as in MTF3, $U = 15\Delta = 0.5J_{\mathrm{H}}$. Bottom row (**d**-**f**): Same as top row but with $U = 300\Delta = 10J_{\mathrm{H}}$. Note that the horizontal axes ($\overline{\varepsilon}/\Delta$) span a different range in each row.

References

1. Thielmann, A., Hettler, M. H., König, J. & Schön, G. Super-poissonian noise, negative differential conductance, and relaxation effects in transport through molecules, quantum dots, and nanotubes. *Phys. Rev. B* **71**, 045341 (2005).

2. Choi, D. J. *et al.* Mapping the orbital structure of impurity bound states in a superconductor. *Nat. Commun.* **8**, 15175 (2017).

3. Ruby, M., Peng, Y., von Oppen, F., Heinrich, B. W. & Franke, K. J. Orbital picture of Yu-Shiba-Rusinov multiplets. *Phys. Rev. Lett.* **117**, 186801 (2016).

4. Ruby, M. *et al.* Tunneling processes into localized subgap states in superconductors. *Phys. Rev. Lett.* **115**, 087001 (2015).

5. Huang, H. *et al.* Tunnelling dynamics between superconducting bound states at the atomic limit. *Nat. Phys.* **16**, 1227–1231 (2020).

6. Perrin, V. *et al.* Unveiling odd-frequency pairing around a magnetic impurity in a superconductor. *Phys. Rev. Lett.* **125**, 117003 (2020).

7. Thupakula, U. *et al.* Coherent and incoherent tunneling into yu-shiba-rusinov states revealed by atomic scale shot-noise spectroscopy. *Phys. Rev. Lett.* **128**, 247001 (2022).

8. Kiršanskas, G., Pedersen, J. N., Karlström, O., Leijnse, M. & Wacker, A. Qmeq 1.0: An open-source Python package for calculations of transport through quantum dot devices. *Comput. Phys. Commun.* **221**, 317–342 (2017).

9. Huang, H. *et al.* Quantum phase transitions and the role of impurity-substrate hybridization in Yu-Shiba-Rusinov states. *Commun. Phys.* **3**, 199 (2020).

10. Georges, A., Medici, L. d. & Mravlje, J. Strong correlations from hund's coupling. *Annual Review of Condensed Matter Physics* **4**, 137–178 (2013).

11. Tsurkan, V. *et al.* Physical properties of $FeSe_{0.5}Te_{0.5}$ single crystals grown under different conditions. *The European Physical Journal B* **79**, 289–299 (2011).

12. Miyake, T., Nakamura, K., Arita, R. & Imada, M. Comparison of ab initio low-energy models for LaFePO, LaFeAsO, $BaFe_2As_2$, LiFeAs, FeSe, and FeTe: electron correlation and covalency. *JPSJ* **79**, 044705 (2010).

13. Schrieffer, J. R. & Wolff, P. A. Relation between the Anderson and Kondo Hamiltonians. *Phys. Rev.* **149**, 491–492 (1966).

14. Wang, Z. *et al.* Evidence for dispersing 1D Majorana channels in an iron-based superconductor. *Science* **367**, 104–108 (2020).

15. Heinrich, B. W., Rastei, M. V., Choi, D. J., Frederiksen, T. & Limot, L. Engineering negative differential conductance with the cu(111) surface state. *Phys. Rev. Lett.* **107**, 246801 (2011).

16. Hatter, N., Heinrich, B. W., Ruby, M., Pascual, J. I. & Franke, K. J. Magnetic anisotropy in Shiba bound states across a quantum phase transition. *Nat. Commun.* **6**, 8988 (2015).

17. Franke, K. J., Schulze, G. & Pascual, J. I. Competition of superconducting phenomena and kondo screening at the nanoscale. *Science* **332**, 940–944 (2011).

18. Farinacci, L. *et al.* Tuning the coupling of an individual magnetic impurity to a superconductor: quantum phase transition and transport. *Phys. Rev. Lett.* **121**, 196803 (2018).

19. Chatzopoulos, D. *et al.* Spatially dispersing Yu-Shiba-Rusinov states in the unconventional superconductor $FeTe_{0.55}Se_{0.45}$. *Nat. Commun.* **12**, 298 (2021).

20. Coleman, P. *Introduction to many-body physics* (Cambridge University Press, 2015).

21. Martiny, J. H. J., Kreisel, A. & Andersen, B. M. Theoretical study of impurity-induced magnetism in FeSe. *Phys. Rev. B* **99**, 014509 (2019).